

Dynamical Motions and Oscillations of a Quiescent Prominence Observed by IRIS and SDO/AIA

Jain Jacob P. T.

National Institute of Technology Calicut

R. A. Maurya (✉ ramajor@nitc.ac.in)

National Institute of Technology Calicut

Safna Banu K.

National Institute of Technology Calicut

Research Article

Keywords: Prominence – Sun, Chromosphere – Sun, Oscillations – Sun, Magnetic fields

Posted Date: May 12th, 2022

DOI: <https://doi.org/10.21203/rs.3.rs-1632954/v1>

License: © ⓘ This work is licensed under a Creative Commons Attribution 4.0 International License.

[Read Full License](#)

Dynamical Motions and Oscillations of a Quiescent Prominence Observed by IRIS and SDO/AIA

Jain Jacob P. T.¹ · R. A. Maurya¹ · Safna Banu K.¹

© Springer ●●●●

Abstract

We studied the dynamical properties of a quiescent prominence using high-resolution observations provided by the Interface Region Imaging Spectroscopy (IRIS) and Atmospheric Imaging Assembly (AIA) onboard Solar Dynamics Observatory (SDO). IRIS's spectroscopic observations helped us compute the Doppler velocity maps in the prominence. The emission measure and temperature maps in the prominence regions are computed using the Differential Emission Measure (DEM) analysis of the EUV observations obtained from SDO/AIA. We employed the local correlation tracking (LCT) to find the plane-of-sky motion in the prominence. The prominence bubble was found to be rotating anti-clockwise with a rotation period of around 60 minutes when viewed from the top of it. We found dynamical motion 20 to 60 km s⁻¹ in the prominence and its rotations. On the other hand, the central part of the prominence was making torsional rotations. This could be associated with upward propagating torsional Alfvén waves along the magnetic field lines. We also found a sizable helical motion in the upper part of the prominence with a linear speed of 6.35 km s⁻¹. Further, the prominence was found to have significant oscillations in the frequency band 1.5 - 2.5 mHz, corresponding to the period range of 7 - 11 minutes with a dominant oscillation for around 10 minutes.

Keywords: Prominence – Sun: Chromosphere – Sun: Oscillations – Sun: Magnetic fields

1. Introduction

Prominences are observed above the solar limb and are extended to coronal heights. They are consisting of cool and dense plasma suspended over magnetic field lines. Prominences can be broadly classified into two groups, quiescent and active. Quiescent prominences have no near active regions and have a longer lifetime (from several days to weeks), while active prominences are observed near active regions and last only for a few hours to days. They have a lower density, weaker magnetic field and lower temperature than active prominences (Labrosse *et al.*, 2010). The quiet prominences can also reach higher in the atmosphere, but the brightness is almost constant or slightly diminishing with height.

The active prominences are eruptive and lead to energetic activities such as solar flares and coronal mass ejections (CME's). The stability of a prominence can be explained with the help of magnetic fields. The frozen-in magnetic field may rearrange an environment to the plasma structure against gravity. A rotational motion in prominence structure changes the

✉ Ram Ajoy Maurya
ramajor@nitc.ac.in

Jain Jacob P. T.
jain'p180130ph@nitc.ac.in

Safna Banu K.
safna'p180029ph@nitc.ac.in

¹ Department of Physics, National Institute of Technology Calicut, Kerala-673601

magnetic field orientation leading to magnetic reconnection. In Addition, the pre-eruption field configuration must be consistent with the observed structure of prominences and account for their gravitational and thermal stability. However, the driving mechanism that leads to the eruption of prominence has not been fully understood.

The observations have shown different types of dynamical motions within prominences such as vertical, horizontal and steady flows, unidirectional and bidirectional flows, and oscillatory movements (Berger *et al.*, 2008; Chae *et al.*, 2008; Jing *et al.*, 2006; Lin, rn Engvold, and Wiik, 2003; Zirker, Engvold, and Martin, 1998). Tornadoes like structures and rotations are also reported earlier (Su *et al.*, 2012; Li *et al.*, 2012; Su *et al.*, 2014). Rotatory motion within a prominence exhibit oscillation in both plane-of-sky and line-of-sight directions (Su *et al.*, 2014). The circular motion of the plasma in the plane-of-sky direction are also interpreted as rotational motion (Li *et al.*, 2012). This can be confirmed if a line-of-sight velocity gradient is present along with the circular motion (Su *et al.*, 2014; Levens *et al.*, 2015). The combined observations of motions along plane-of-sky and line-of-sight direction is rare. Simultaneous spectral and imaging observations can be used to validate such motions.

The dynamical motions in the prominence are three-dimensional, which cannot be confirmed from two-dimensional imaging. A line-of-sight movement in the prominence can help us approve the prominence's three-dimensional activities. One can find this motion in the prominence using the Doppler measurements. The Doppler velocity at a point is blue-shifted for motion towards the observer and red-shifted for motion away from the observer. A line connecting two points on opposite sides of a prominence spine having a Doppler velocity gradient shows the rotation of prominence structure (Kucera, Ofman, and Tarbell, 2018). Previous studies interpreted the rotation as photospheric vortices under the Prominence (Su *et al.*, 2012) and associated flares and EUV waves (Panesar *et al.*, 2013).

The prominences show oscillatory motions caused by their natural plasma oscillations or by the waves coming from the photosphere or due to perturbations in the prominence itself due to other dynamical activities. The oscillatory motions in a prominence structure may help us to understand the coronal heating problem and propagation of MHD waves (Berger *et al.*, 2008; Lin *et al.*, 2007). The prominence oscillations can be classified according to period, oscillatory amplitude, the polarization of motions, prominence shape, exciter etc. (Arregui, Oliver, and Ballester, 2018). The observed period of oscillations in prominences ranges from one minute to a few hours (Engvold, 2007). The propagation of MHD waves across a prominence may induce oscillatory motions in individual threads as observed in some studies of quiescent prominence (Lin *et al.*, 2007) and active region prominence (Okamoto *et al.*, 2007). The detected periodicity can be explained with the help of theoretical modelling (Oliver and Ballester, 2002; Ballester, 2005). The propagating waves are interpreted by linear magneto-acoustic waves (Diaz, Oliver, and Ballester, 2002). Transverse displacements of the flux tubes are interpreted by kink wave modes (Edwin and Roberts, 1983; Terradas *et al.*, 2008). Similar oscillations are observed in the coronal loop, and the physical conditions of plasma are found by MHD seismology (Nakariakov and Ofman, 2001).

The prominence rotation can be detected from the Doppler velocities measured at different locations in the prominence (Schmieder *et al.*, 2014; Okamoto, Liu, and Tsuneta, 2016). However, the driving mechanism of rotation of prominences is still unclear, and more study is required for the detection of the non-thermal process. Several still-unsettled issues motivate us to study the prominence, such as support and stability against gravity, mass motions, radiative losses, magnetic field, formation and disappearance, etc.

This paper provides studies of the dynamical motions and oscillations in a quiescent prominence. The rest of the paper is arranged as follows: We describe the observation and data analysis in Section 2. Section 3 presents the results and discussion. We summarize our results in Section 4.

2. The Observational Data and Analysis

We used the high-resolution observations provided by the space-borne observatories, such as the Atmospheric Imaging Assembly (AIA) (Lemen *et al.*, 2011) onboard Solar Dynamics

Observatory (SDO) and the Interface Region Imaging Spectrograph (IRIS) (Pontieu *et al.*, 2014).

SDO/AIA provides intensity images in Ultra-Violet (UV), such as, 1600Å, 1700Å and in Extreme Ultra-Violet (EUV), such as, 94Å, 131Å, 171Å, 193Å, 211Å, 304Å and 335Å wavelengths. These data have a pixel and temporal resolutions of $0''.6$ and 12 s, respectively. The multi-wavelength observations help us to study the plasma properties at different heights in the solar atmosphere. We computed the temperature and emission maps using the AIA's six EUV wavelengths by applying the Differential Emission Measure (DEM) method as discussed by Aschwanden *et al.* (2013).

The IRIS provides imaging (or slit-jaw images (SJI)) in four broadband filters, such as, 1330 Å, 1400 Å, 2796 Å and 2832 Å, as well as, spectroscopic observations in the Near Ultra-Violet (NUV 2783–2834 Å) and the Far Ultra-Violet (FUV 1332–1348 Å & 1390–1406 Å) wavelength bands. IRIS/SJI observations have a pixel resolution of $0.33''$ along both the x-direction (scan direction) and y-direction (perpendicular to the scan direction) with a cadence of 20.8 s. Generally, the spectral observations are taken with pixel resolutions of 0.026Å and $0.33''$ along the wavelength (λ) and y-direction, respectively. But it varies along the x-direction. It depends upon the number of rasters taken in a given field of view. For this prominence, the raster and the slit-jaw observations were taken for the field-of-view of $127'' \times 182''$ and $295'' \times 182''$, respectively, around the heliocentric position ($833''$, $573''$). The prominence was observed using 64 raster-positions, resulting a coarse pixel resolution of $2''$ along the x-direction, during 12:41 UT to 13:36 UT on December 17, 2015. In this observation period of ~ 1 hour, we have only 10 data cubes ($x \times y \times \lambda$) due to a long scanning time of 333 s of the above field-of-view. For this work, we have only used the Level-2 IRIS observations that are corrected for the dark currents, flat fielding and geometrical effects (Pontieu *et al.*, 2014).

The line-of-sight and plane-of-sky motions in the prominence are studied using the Doppler velocities and the optical flows. The Doppler velocities in the prominence is computed using the Solar-Soft routine, `iris_get_mg_features_lev2.pro`, from the Mg II k spectrogram obtained from the IRIS observations. Further, we have chosen the optically thin SDO/AIA 193 Å intensity images to find the plane-of-sky motion using Local Correlation Tracking (LCT, Welsch *et al.*, 2004) where the prominence threads are discernible. We found that the 30 pixels sigma value returns reasonable velocities when applied to two intensity images observed at a time difference of 4 minutes for the LCT computations.

We study the prominence oscillations using the high-resolution intensity observations provided by the IRIS. The Doppler velocities can provide better information about the oscillatory phenomenon in the prominence. But, only ten spectral observations are available for this prominence during 12:41 UT–13:36 UT that give us poor spatial resolutions along the scanning direction. Therefore, we have utilized the IRIS/SJI intensity images in Mg II and Si IV wavelengths.

The power in the prominence is analysed using the Fourier transform of the intensity time series. But, a time-dependent frequency signal cannot be determined using the Fourier transformation. For this, we have used the wavelet transform, as discussed by Torrence and Compo (1998), of the IRIS/SJI at wavelengths of Mg II 2796 Å, Si IV 1400 Å and SDO/AIA 193 Å.

3. Results and Discussions

Results of our analysis of the prominence are shown in Figures 1 – 9.

3.1. The Quiescent Prominence

The quiescent prominence was seen at the northwest solar limb on December 17, 2015 (see Figure 1f). It is formed from the evolution of two magnetic threads, T_1 and T_2 , observed in SDO/AIA 193Å at 9:00 UT on December 15, 2015. Initially, one of the threads T_2 was seen close to the limb and the other T_1 away from the limb, see Figure 1 (a) - (c). As time progressed, the magnetic thread T_1 moved close to the limb due to solar rotation. On December 17, 2015, around at 3:00 UT, another magnetic thread T_3 was observed in between

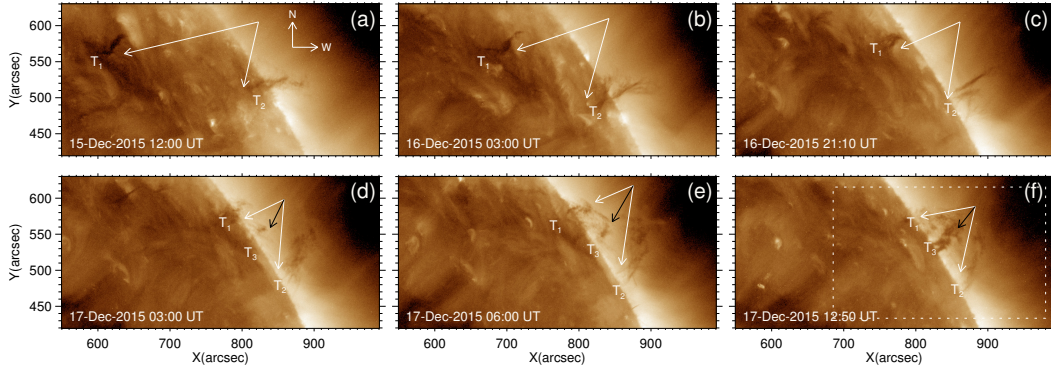


Figure 1. SDO/AIA 193Å intensity images during the formation of the prominence. The arrowheads labelled with T_1 and T_2 mark the magnetic threads that lead to the formation of the prominence. The label T_3 in the panels (d) – (f) marks the third magnetic thread that evolved to the central part of the prominence. The dashed rectangular box in panel (f) represents the field-of-view of IRIS/SJI observations.

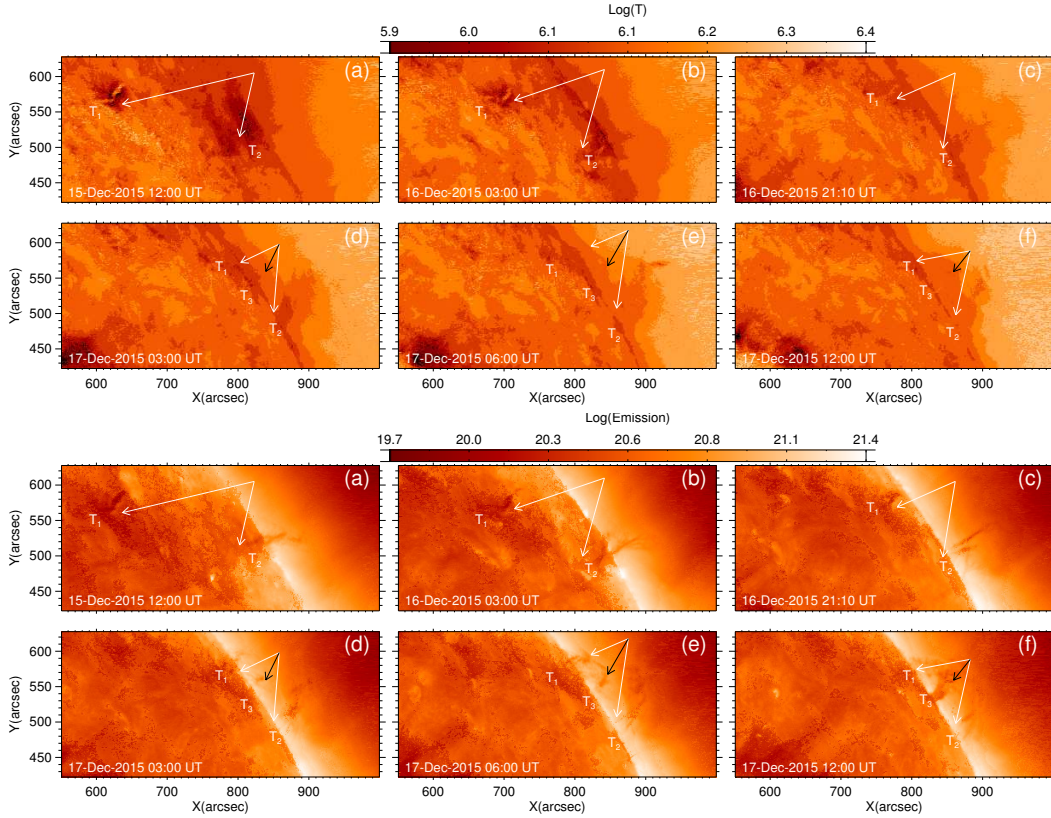


Figure 2. Similar to Figure 1 but containing the physical parameters, temperature (top two rows) and emission measure maps (bottom two rows).

the threads T_1 and T_2 , see panel (d). These threads were seen to form a closed loop, and after three hours, a complete prominence structure was found to be established. After a few hours, T_3 evolved into a sizable magnetic thread and later on, it split into two that are seen as two legs L_1 and L_2 of the prominence (see Figure 4f). They can be seen more clearly in the panels (c) – (g) of Figure 4. This prominence is found to have a geometrical heights of 59.50 Mm and 44.8 Mm, diameters 119.5 Mm and 93.5 Mm in the wavelengths 304Å and 193Å, respectively. After around a half-day at 18:00 UT the prominence structure was found to be decaying, and the next day at 8:00 UT, it almost vanished from the solar atmosphere.

This prominence was fully covered by the IRIS imaging and spectroscopic observations which helped us to investigate its important properties. A sample of IRIS observations of the prominence is shown in Figure 3. This prominence was well observed in IRIS spectral lines MgII and SiIV. Therefore, we expect a temperature of the prominence in the

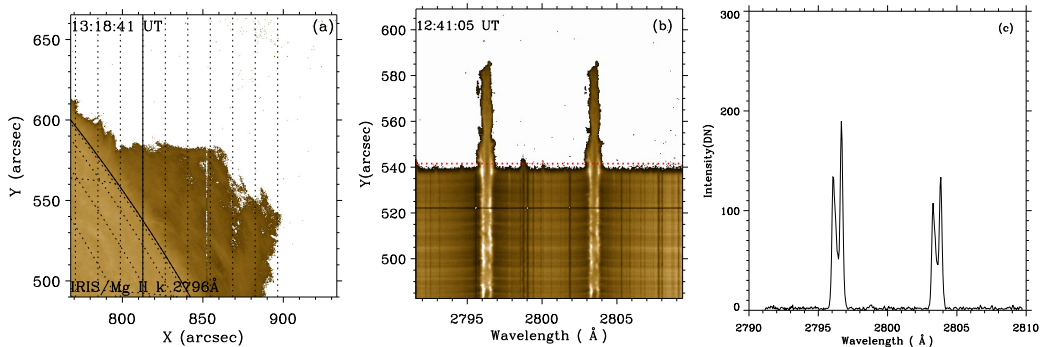


Figure 3. (a) Logarithmic intensity image of the prominence observed by the IRIS slit-jaw in the Mg II k line (2796 Å). Vertical dashed lines represent 10 (out of 64) raster positions with a gap of 7 as observed by the IRIS spectrograph. (b) A sample of IRIS spectrogram at the x-position 812'' as shown by a solid vertical line in panel (a) and observed at 12:41:05 UT. (c) A spectral line profile in the prominence at the spatial position (812'', 542''). The y-position of the spectral profile is marked with a red dashed horizontal line in the middle panel (b).

range $10^4 - 10^5$ K. The temperature maps obtained from the DEM analysis are shown in Figure 2. The emission maps resemble the properties of the magnetic threads as seen in the SDO/AIA 193 Å intensity images (see Figure 1). The temperature maps show that the regions of threads T_1 , T_2 and T_3 are cooler than their surroundings. From an animation of the temperature maps, we found a flow of cooler plasma rising from the threads T_1 and T_2 upward and then falling into the region where the thread T_3 is located. These motions of plasma resulted in the formation of the prominence bubble.

A spectrogram of observations of the prominence in IRIS Mg II k & h wavelength bands is shown in Figure 3(b). Above the spatial position, $y = 540''$, the intensity is only observed close to the wavelengths 2796 Å and 2803 Å because of the emissions from the Mg II ions in the prominence. The emissions from the region below $y = 540''$ correspond to the lower solar atmosphere. The intensity profile corresponding to the position, $y = 542''$, is shown in Figure 3(c), which shows emission profiles specifically in the Mg II k & h. We find a reversal near the cores of both the spectral lines, indicating that the prominence is optically thick in these wavelength bands. Since the prominence is optically thick in the spectral line Mg II, we cannot see its detailed structure (see Figure 3a). On the other hand, it is optically thin in SDO/AIA 193 Å, allows us to observe the fine scale features of the prominence (see Figure 4).

Figure 4 shows the temporal evolution of the prominence in SDO/AIA-193 Å during 12:31:06 UT – 13:33:06 UT. A careful analysis of these observations showed dynamical motions in different parts of the prominence: rotation of the entire prominence envelop around the reference line LM, torsional oscillations of magnetic threads in the central part of the prominence, plasma flows from the threads, T_1 and T_2 , regions to upward and combining with the spine region of the prominence, helical motions in the topmost of it, etc.

3.2. Rotation of the Prominence

From an animation of SDO/AIA 193 Å intensity images, we found that the entire prominence is rotating anti-clockwise when viewed from the top. At the same time, its central part makes a torsional rotation around its axis (LM, shown in Figure 4d).

To show the rotational motion of the prominence bubble, we have constructed space-time intensity maps along six different curves, $S_0 - S_5$, across the prominence (see Figure 4(f)), by combining the intensities along these curves as a function of time. Thus, the constructed maps are shown in Figure 5. The horizontal dashed lines marked the intersection locations of the line segment LM and the slits. The map region above (below) the dashed line corresponds to the north (south) of the line segment LM. The dark trend with a positive (negative) slope above the dashed line shows the clockwise plasma motion around the reference line LM of the front (back) part of the prominence. For example, in the space-time intensity map for the slit S_0 , there is a dark thread with a positive slope above the horizontal dashed line, which represents the counter-clockwise motion of the backside of the prominence. In the slit S_3

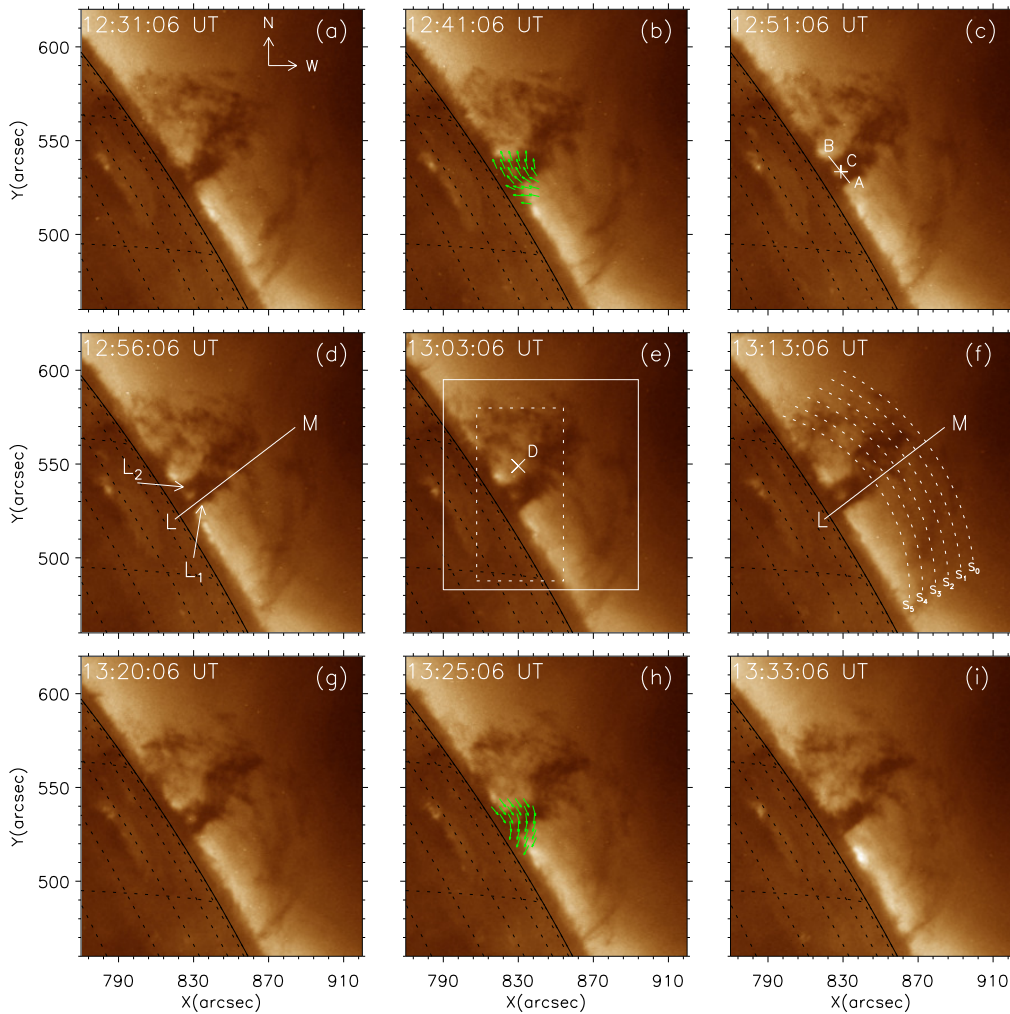


Figure 4. Temporal evolution of the prominence as observed by SDO/AIA 193 Å. Arrows with labels ‘ L_1 ’ and ‘ L_2 ’ in panel (d) mark the two legs of the prominence near the solar limb. The vertical line LM represents a reference line for describing the rotation of the prominence. The green vectors in panels (b) & (h) show plane-of-sky motion in the prominence obtained from an LCT analysis. The line AB in panel (c) marks the position on the prominence where a space-time map is extracted and shown in Figure 6(a). The point ‘+’ labelled with a label ‘C’ on the line AB marks a position where intensity variation as a function of time is extracted and plotted in Figure 6(b). Rectangular boxes with solid and dashed lines represent the regions used to analyze the Doppler velocity (Figure 10) and power spectra (Figure 11). The point D(830'', 549'') marked by a cross symbol ‘x’ represents the position where oscillations wavelet power is computed and shown in Figure 12. In panel (f), the dashed curves $S_0 - S_5$ represent the positions along which space-time intensity maps are constructed (see Figure 5) to show the prominence rotation.

there are downward motions from the central part of the prominence showing anti-clockwise rotation of the front plasma. The speed of these features ranges between $20 - 60 \text{ km s}^{-1}$. One should note that features showing clockwise motions are caused by plasma motion around LM in the other side of the prominence. We have further confirmed this from the Doppler velocity maps in the prominence (see Figure 10). From the Dopplergrams, we found patterns of red-blue-red-blue shifts in the prominence region as we move from the limb radially outward. Similar patterns of Doppler shift in all maps show the motion of plasma away and towards us due to rotation of the prominence.

Further, to show the torsional motion in the central part of the prominence, we labelled the central magnetic threads as its legs L_1 and L_2 . We find a rotation of the prominence leg L_2 around the line segment LM. For this, we computed a space-time intensities map along a line segment between the points A(833.657'', 527.41'') and B(822.257'', 541.81'')

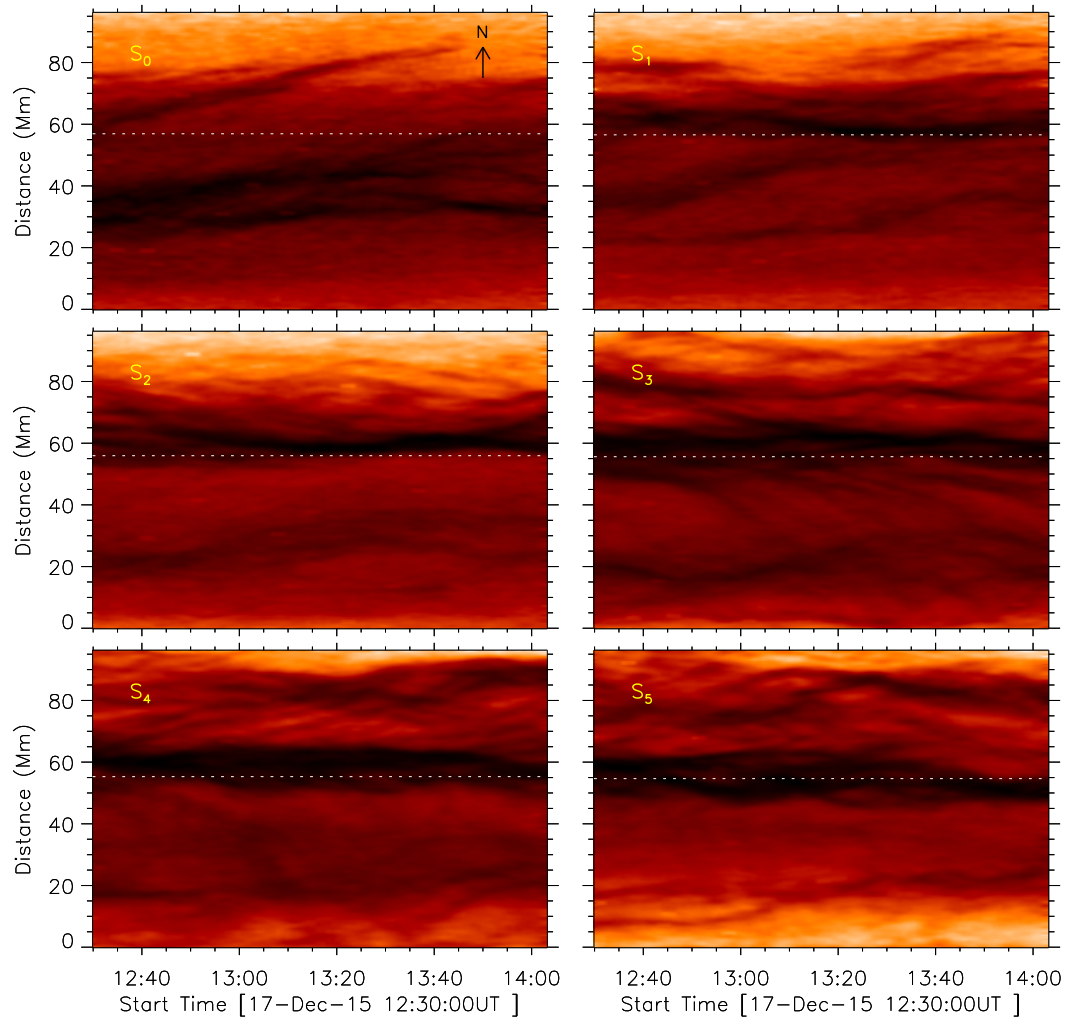


Figure 5. Space-time intensity map across the prominence bubble for six slit positions $S_0 - S_5$ (see Figure 4f), where a horizontal dashed line represents the position of the intersection of slits and the line segment LM.

(see Figure 4c) which is perpendicular to the axis (LM, see Figure 4d). The space-time map is constructed by stacking the intensity along with AB as a function of time. Thus, the constructed intensity space-time map is shown in Figure 6(a). The torsional motion is evident from this map. The two dark features above and below the horizontal dashed line in the map represent the intensity in the legs of the prominence. The white curves mark the darkest spatial positions as a function of time which help us to identify the up-down variation of the dark feature in the space-time map. The leg L_1 is almost stationary as there is no significant up-down variation of dark features in the space-time map, while there is a substantial change in the spatial position of the leg L_2 . In the space-time map, the dark feature initially moves towards the point B then downward and repeats a similar motion after 13:05 UT. This shows the torsional rotation of the leg L_2 around the leg L_1 , first clockwise and then anti-clockwise when viewed from the top of the prominence.

The intensity profile along the dashed horizontal line in the space-time map is shown in the bottom panel (Figure 6b), where two peak intensity positions correspond to the time of rotation of the leg L_2 when it is separated maximum from the leg L_1 . The peak intensity positions, marked by two vertical lines, are separated with a difference of 30.6 minutes. The intensity variation is caused by a torsional rotation of the prominence leg L_2 around LM. Conversely, the south leg L_1 did not exhibit such motion. We found that the two bright regions in the space-time map (see Figure 6(a)) is located in the same positions between two consecutive 180° rotations, *i.e.*, the north leg rotated 180° about the south leg of prominence then 180° in the opposite direction. Considering two successive peak positions

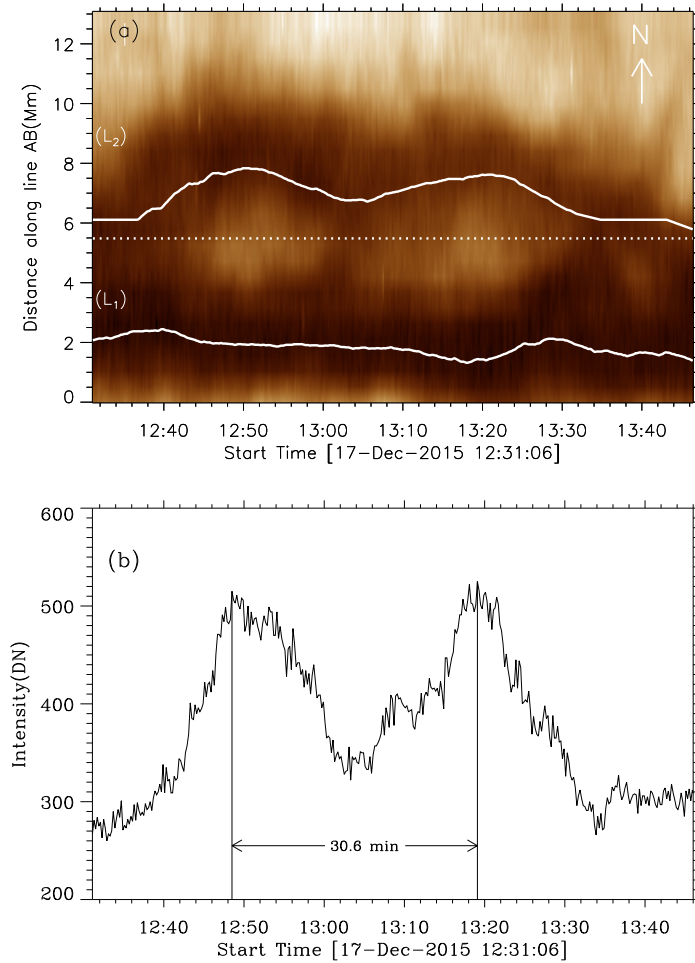


Figure 6. Top panel (a) shows the space-time intensity map along the line AB (see Figure 4c) across the prominence legs, ‘ L_1 ’ and ‘ L_2 ’. White solid curves show the minimum intensity positions as a function of time. The horizontal dashed line, corresponding to the spatial position ‘C’ marked by the symbol ‘+’ in Figure 4(c), on the map taken as a reference position along the intensity profile shown in the bottom panel (b). The solid vertical lines mark the maximum intensity positions at two different times with a gap of 30.6 minutes.

due to a rotation of 180° the angular speed can be estimated as $\omega = \Delta\theta/\Delta t = \pi/1836 = 0.001711 \text{ rad s}^{-1}$. A distance of 6.58 Mm separates the two legs. Then the tangential speed of the rotating leg L_2 will be 11.2 km s^{-1} .

We have also tracked the horizontal motions of prominence features using the LCT analysis. We find that the magnitude of the horizontal velocity varies in the range of $10 - 20 \text{ km s}^{-1}$, which is in the order of prominence rotation. This suggests some relation between the rotation of the prominence leg L_2 and the plane of sky motion in the prominence. The horizontal motions in the prominence leg’s region obtained from the LCT analysis is shown in panels (b) and (h) of the Figure 4 for two different times 12:41:06 UT and 13:25:06 UT, respectively. We found that the velocity vectors initially pointed towards the northeast direction and further at 12:54 UT changed to the southwest direction. This confirms the rotational motion of the prominence leg, initially clockwise then anti-clockwise sense when viewed from above the prominence. The line-of-sight component of this torsional rotation of the leg L_2 has been further confirmed from the Doppler observations.

The Doppler velocity profile along the line AB in Mg II k, for two different times 12:43:53 UT and 13:22:44 UT, are shown in Figure 7. The magnitude of the Doppler velocity along the line AB ranges between $\pm 10 \text{ km s}^{-1}$, which matches with an order of magnitude of the tangential velocity of the prominence leg rotation as discussed earlier in this section. In order to find the Doppler velocity gradient as a function of space along the line AB, we have fitted a straight line through the data points. From panel (a), we find a positive slope

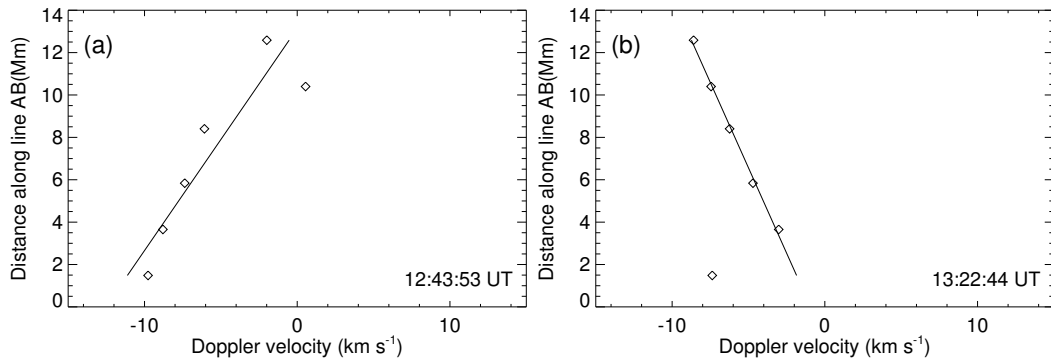


Figure 7. Doppler velocity variations along the white line AB (see Figure 4c) computed from the IRIS spectral line Mg II k at times 12:43:53 UT (a) and 13:22:44 UT (b). The solid line represents the linear least-square fit through the data points (marked with symbol ‘◇’).

in the fitted line that changed to a negative later. It indicates the clock wise rotation of the prominence while looking from the top of the prominence. Later in panel (b), the Doppler shifts along the line AB changed to opposite sense. It shows an anti-clockwise motion in the prominence leg. It means that initially, the prominence leg rotated clockwise and then changed the direction of rotation to anti-clockwise after half an hour. Similar results from the plane-of-sky motion and Doppler velocity gradient confirms the presence of rotational rotation of the prominence’s leg L_2 about the leg L_1 . These dynamical motions in the prominence are illustrated by a schematic diagram in Figure 8.

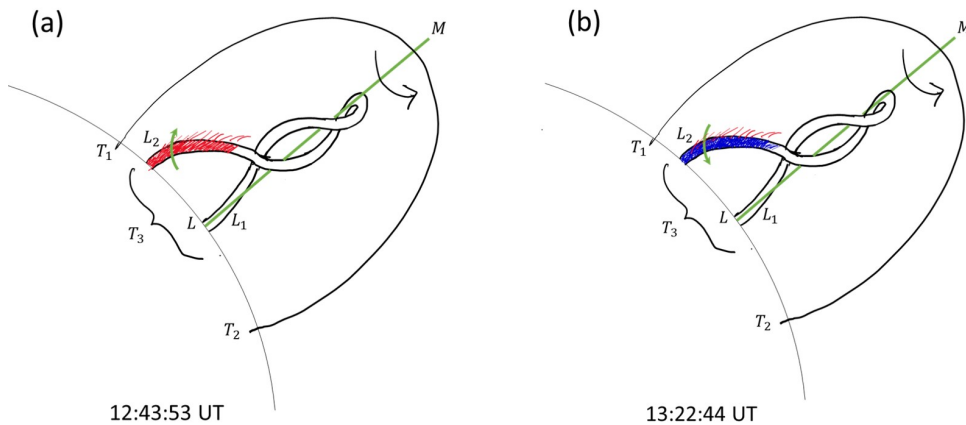


Figure 8. An schematic representation of rotation of the prominence at two different times, 12:43:53 UT (a) and 13:22:44 UT (b), as revealed from the SDO/AIA intensity and IRIS Doppler velocity observations. Inverted ‘U’ shape represents the prominence envelop that is formed by the magnetic threads T_1 and T_2 anchored in the photosphere. L_1 and L_2 inside inverted ‘U’ shape, mark the prominence legs, formed by splitting of the magnetic thread T_3 , where red and blue colors represent the redshift and blueshifts, respectively. The line LM represents the axis of rotation of the prominence legs.

3.3. Helical Motions in the Prominence

We found upward helical motion in the upper part of the prominence intermediate regions labelled with ‘B’ and ‘R’ positions (Figure 9a). But this motion cannot be explained using the intensity images alone. The line-of-sight Doppler motions and the intensity images can help us understand the three-dimensional helical motion in prominence. To illustrate this motion, we divided it into two components, i) northeast motion along the line PQ in the plane-of-sky, and ii) line-of-sight motions regions in the ‘R’ and ‘B’ sides PQ (see Figure 9a).

While analyzing a sequence of IRIS/SJI Mg 2796 Å intensity images, we found the north-east motion of prominence threads, marked by an arrow PQ in Figure 9(a). We constructed a space-time intensity map to show this motion by stacking the intensity along the line segment PQ as a function of time. Thus the constructed map is shown in the right panel (b)

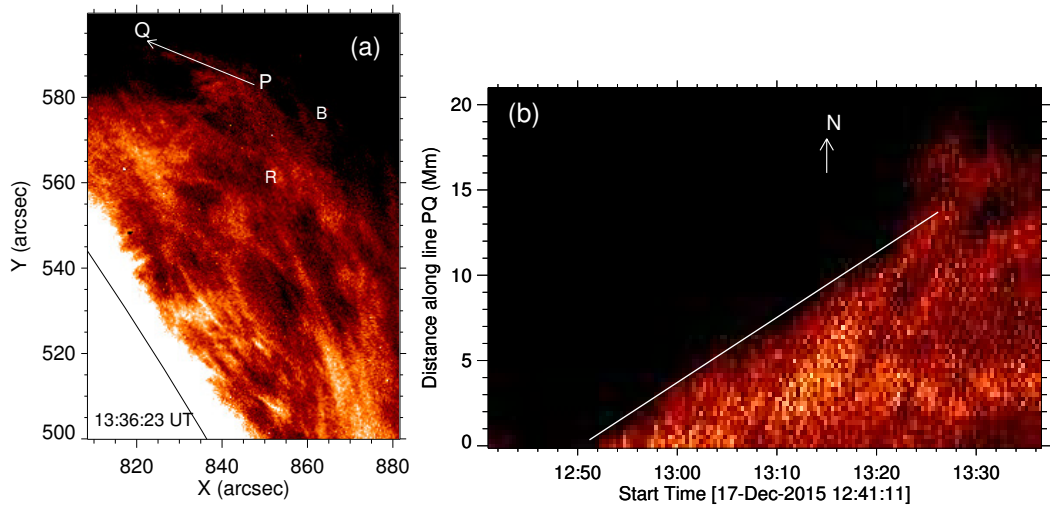


Figure 9. (a) Intensity image of the quiescent prominence as seen in the IRIS/SJI-2796Å wavelength. The arrow PQ marks the upward motion in the prominence. The regions marked with ‘R’ and ‘B’ show the prominence’s positions with blueshift and redshift, respectively (see Figure 10). (b) Space-time intensity map along the line PQ. The solid white line is drawn through the upper part of the prominence along the line PQ.

of Figure 9. In this map, the prominence features appear after 12:50 UT and rise towards the point ‘Q’ as time progresses. This clearly shows the motion of the prominence plasma in the northeast direction. We estimated the speed of this upward motion to be 6.35 km s^{-1} by fitting the top part of the prominence in the space-time intensity map (Figure 9b).

The line-of-sight motion in the prominence is analysed using the dopplergrams constructed from the Mg II spectrograms obtained from the IRIS observations. An image mosaic of the dopplergrams in prominence for different times is shown in Figure 10. The magnitude of Doppler velocity in the prominence regions is found to vary in the range of $\pm 30 \text{ km s}^{-1}$.

In the previous discussions, we have seen upward plane-of-sky motion in the top part of the prominence between the points ‘R’ and ‘B’ (see Figure 10). This motion is tracked using an optical flow method (LCT), and the computed velocities are overlaid on the Doppler maps. The horizontal motion is consistently upward during the rotation of the prominence regions marked by ‘B’ and ‘R’. We find blueshift and redshift in the same IRIS Mg II spectral line, which shows prominence motion towards the observer and then away, respectively. Combining motions obtained from the LCT analysis, dopplergrams and space-time maps, we conclude anti-clockwise upward helical motion when viewed from the north of the solar disc. This helical motion has been consistently observed during 12:49 UT – 13:33 UT.

3.4. Oscillations in the Prominence

The oscillations in the prominence are studied using the Fourier analysis of the IRIS/SJI intensity images observed during the 12:41 UT - 13:36 UT. First, we computed the Fourier power spectra for every spatial position in the region marked by a dashed rectangular box in Figure 4(e). Then the power is averaged in six frequency bands, 0.5-1.5 mHz, 1.5-2.5 mHz, 2.5-3.5 mHz, 3.5-4.5 mHz, 4.5-5.5 mHz and 5.5-6.5 mHz. Thus the power maps constructed in six frequency bands are shown in Figure 11 for two wavelengths, Mg II 2796Å (left panel) and Si IV 1400Å (right panel). Note that the more considerable power along the vertical lines in the frequency band 2.5-3.5 mHz is caused by the IRIS raster scanning with a cadence of 333 s (or 3 mHz), and its harmonic appears in the higher frequency band 5.5-6.5 mHz too.

In both the wavelengths, the maximum power is located in the disc regions. There are dominant powers close to the solar limb compared to the higher atmosphere in all the frequency bands. The height of the power region above the limb decreases on increasing the frequency band, *i.e.*, larger frequencies are trapped close to the solar limb.

In the prominence, the Fourier power is largest in the low-frequency band 0.5 – 1.5 mHz and smallest in the high-frequency band 5.5 – 6.5 mHz in both Mg II and Si IV. The power is found to be decreasing with increasing the frequency. In Mg II, there is large power in the

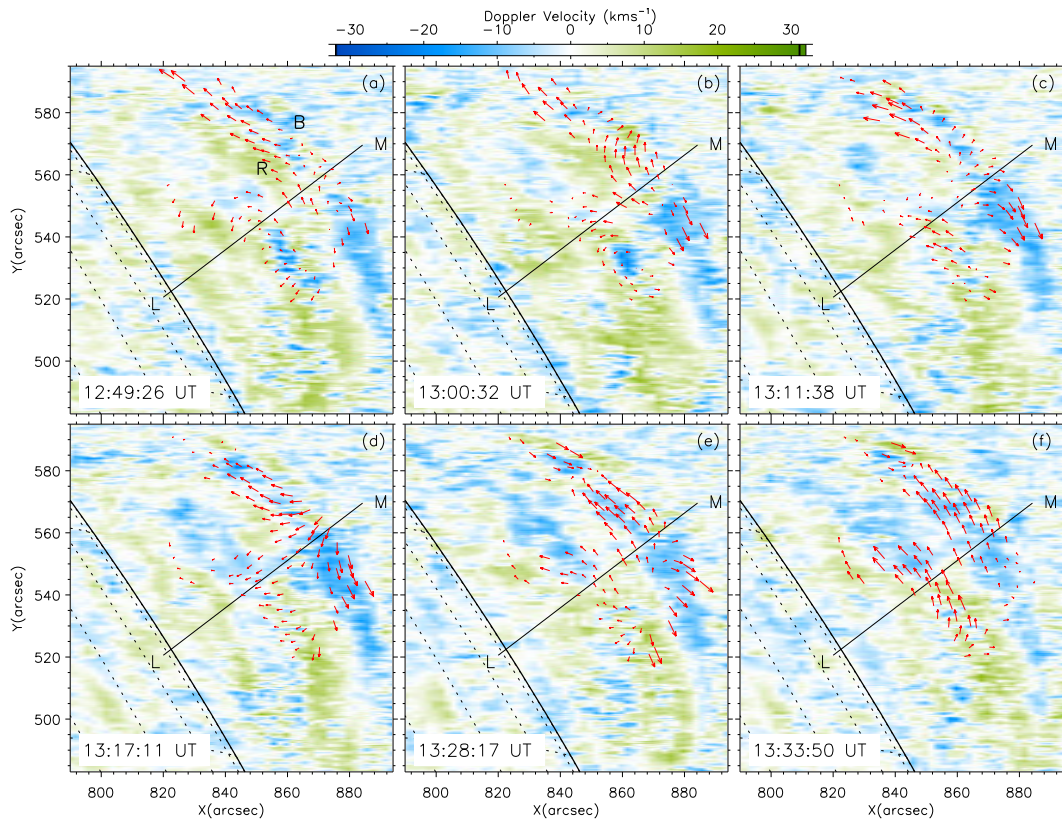


Figure 10. Temporal evolution of the Doppler velocity in the prominence obtained from the line-center of the IRIS Mg II k spectrograms. The red vectors represent the plane-of-sky motion in the prominence obtained from an LCT analysis of SDO/AIA 193Å images. The labels ‘B’ and ‘R’ mark the prominence regions with blue and red Doppler shifts, respectively. The region of the Doppler velocity maps is marked by a solid rectangular box in Figure 4(e). The line segment LM represents reference position as shown in the Figure 4 (d) & (f).

frequency bands 0.5 – 1.5 mHz and 1.5 – 2.5 mHz, low power in the frequency band 2.5 – 3.5 mHz, and no significant power is seen in the higher frequency bands in the prominence regions. In Si IV, there is a considerable power only in the central part of the prominence in the first three frequency bands, see Figure 11 (right panel). One should note that the prominence is rotating anti-clockwise when viewed from the top, and associated power may be reflected in the power spectra. The high powers in the frequency band 0.5 – 1.5 mHz corresponding to the period range 11 – 33 minutes that is associated with the half of the prominence rotation period (~ 60 min) shown in the intensity space-time map across the prominence leg in Figure 6.

The oscillations in the prominence may be time-dependent, which cannot be determined from the Fourier power maps. We have used the wavelet transformations to investigate the time-dependent frequencies in the prominence. A wavelet power spectra in Mg II 2796Å for a prominence position P(830'', 549'') marked by a cross symbol ‘×’ in Figure 4(e), is shown in Figure 12. In this spectra, we have only shown the power for the period below the 15 minutes as there is a strong power close to 30 minutes associated with the rotation of the prominence. The wavelet spectra show a dominant power for the ~ 10 minutes period during first ~ 40 minutes with a confidence level of 95%, see Figure 12(b). It can also be seen clearly in the global wavelet spectra, see panel (c). This period was also detected in the frequency band, 1.5 – 2.5 mHz, of the Fourier power map, see Figure 11. Maps show significant powers for periods ~ 3.5 and ~ 5.5 minutes. But in the global spectra, they are suppressed by the dominant peak associated with ~ 10 minutes. However, these periods are not seen clearly in the Fourier power maps in the corresponding frequency bands 4.5 – 5.5 mHz and 2.5 – 3.5 mHz, respectively.

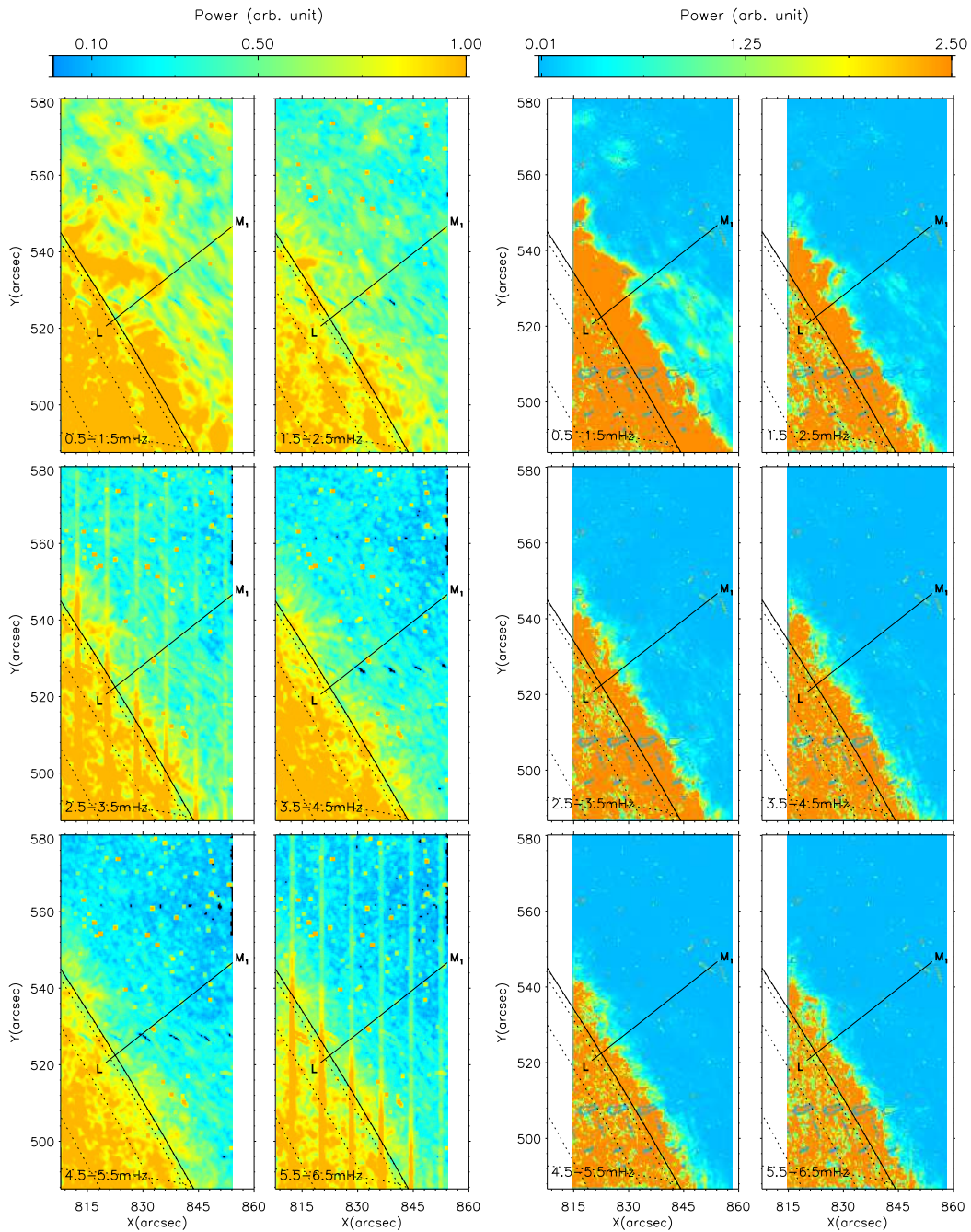


Figure 11. Fourier power maps of intensity images in logarithmic scale of the prominence, as observed by the IRIS/SJI in Mg II 2796 Å (left) and Si IV 1400 Å (right) wavelengths, in six frequency bands. The power map region is marked with a dashed rectangular box in Figure 4(e).

4. Summary and Conclusion

We study the dynamical motions in a quiescent prominence using imaging and spectroscopic observations provided by space-based observatories such as SDO/AIA and IRIS. This prominence was located at the west limb formed from the evaluations of three magnetic threads observed a couple of days before. An upward motion of cool plasma is seen to be rising from two magnetic threads and returning into the region in between them, resulting in the formation of the prominence bubble.

The prominence has a geometrical height of 44.8 Mm from the photosphere and diameter of 93.5 Mm at its base in the wavelength 193Å. This prominence is seen in several EUV channels of SDO/AIA and FUV & NUV of IRIS. The Mg II h & k lines are formed at

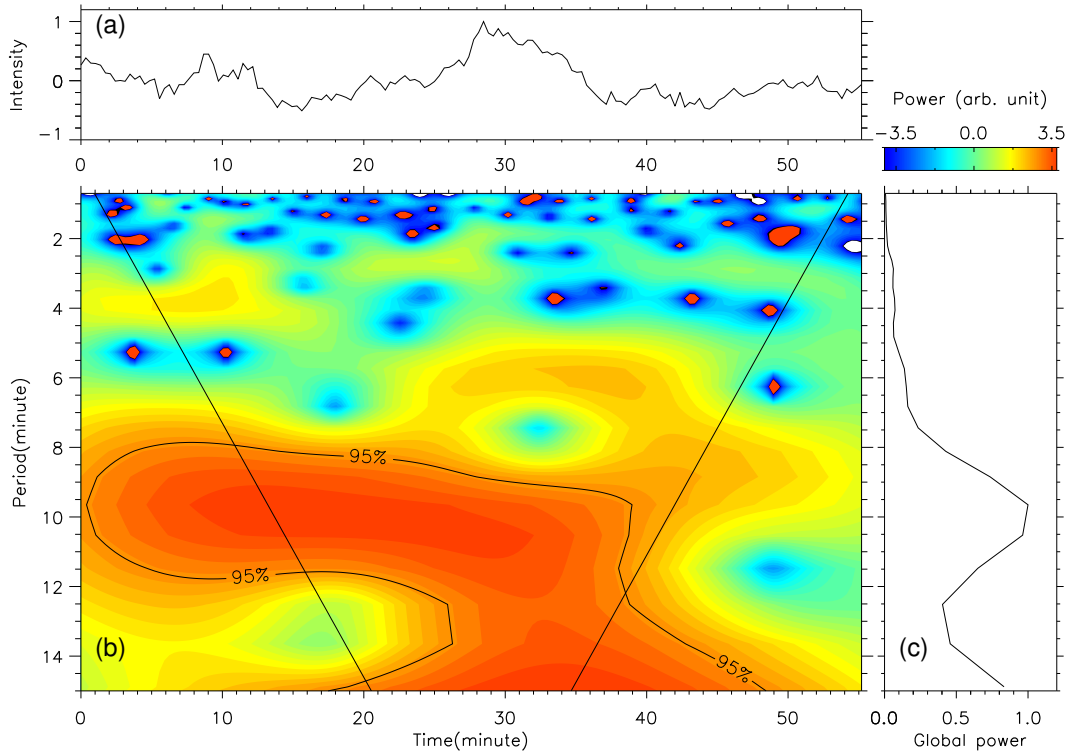


Figure 12. (a) Intensity profile at a position D(830'', 549'') in the prominence (see Figure 4e) observed in IRIS/SJI Mg II 2796Å wavelength. (b) Wavelet power map in logarithmic scale of the intensity profile (a). The power map is constructed by filling 35 contour levels generated between the minimum and maximum values of the wavelet power with a geometric spacing. The solid contour represents the 95% confidence level, and the slanted lines mark the cone of influence. (c) Global wavelet power spectra averaged over time.

chromospheric temperature, and a temperature of $10^4 K$ is expected in this prominence. These lines showed reversed profiles in their cores that indicates optically thick emissions, in these wavelength bands, from the prominence.

We found three kinds of rotatory motions in the prominence: anti-clockwise rotation of the prominence's bubble, torsional rotation of one of its legs around the other leg when observed from the top, and northward helical motion. The prominence bubble is rotating with a period of ~ 1 hour about its axis. That resulted a tangential speed of $\sim 60 \text{ km s}^{-1}$ around at the mid of the prominence. But the moving leg is found to be rotating initially in the clockwise during the first half an hour and then anti-clockwise sense with an angular speed of $0.00171 \text{ rad s}^{-1}$ that gives a tangential speed of 11.2 km s^{-1} near the solar limb. This has also been confirmed from the Doppler velocity measurements in the legs' positions. The Doppler velocity increases from the south leg to the north leg of the prominence, and after half an hour, it reversed. In other words, we found an opposite Doppler velocity gradient, between the leg's positions, during reverse rotations. The difference of Doppler speed of $\sim 11 \text{ km s}^{-1}$ at the two legs matches well with the tangential speed. From an LCT analysis, changes in plasma flow direction are observed after half an hour, similar to Doppler velocity gradient. Thus, combining the plane-of-sky motions from the optical flows and the line-of-sight motions from the Doppler velocities, we conclude a torsional rotation of the prominence's leg. Doppler velocities gradient across the prominence leg have been reported earlier in another rotating prominence (Levens *et al.*, 2016) and are compared with angular frequency obtained from the plane-of-sky observations (Su *et al.*, 2014). The torsional rotation of the prominence leg could be caused by the upward propagating torsional Alfvén waves. Similar patterns of Doppler velocity from Mg II and Si IV, suggests the co-existence of cold and hot plasma in a rotating structure and proves the presence of the Prominence-Corona Transition Region (Su *et al.*, 2014).

In addition, we found helical motion in the top part of the prominence with an upward line speed of 6.35 km s^{-1} . This part is visible in the dopplergram of IRIS Mg II 2796 Å as blue-shifted and red-shifted plasma. It may be related with the counter-streaming flows in

the prominence. Earlier studies proposed that such motions could be caused by fast magneto-sonic wave pulses (Schmieder *et al.*, 2013), kink oscillation (Lin *et al.*, 2009) and changes in the magnetic field configuration (Okamoto, Liu, and Tsuneta, 2016).

The time series analysis of prominence's intensity showed larger power close to the solar limb and it decreases with frequency. The power maps of Mg II and Si IV are quite different because of their formation heights, the chromosphere and the prominence corona transition region (PCTR), respectively. We found that the oscillation power in the prominence ranges between 7 – 11 minutes for SDO/AIA 193 Å and IRIS in Mg II 2796 Å & Si IV 1400 Å intensity images. Lin *et al.* (2007) proposed such fluctuations could be related to Alfvén waves propagating along magnetic flux tubes. The Alfvén waves have a speed close to sound speed in filament plasma due to low magnetic field strength. But we did not identify any travelling wave in the prominence. Also, the oscillations in the plane of sky did not match the period of oscillation obtained from the power spectrum in the frequency range of 1.5 mHz to 2.5 mHz. The periods calculated from power spectrum analysis may be due to line-of-sight oscillations. The oscillations are better resolved in the Doppler observations than intensity images. But for this prominence, we had only ten dopplergrams that could not be used for the time-series analysis. We plan to study waves and oscillations in some other observations of prominences which can be used to compute better samples of dopplergrams.

Acknowledgments IRIS is a NASA small explorer mission developed and operated by LMSAL with mission operations executed at NASA Ames Research Center and major contributions to downlink communications funded by ESA and the Norwegian Space Centre. AIA data are courtesy of NASA's SDO and AIA science team. One of the authors, RAM, acknowledges support from the NITC-FRG.

References

- Arregui, I., Oliver, R., Ballester, J.L.: 2018, Prominence oscillations. *Liv. Rev. Solar Phys.* **15**(1). DOI.
- Aschwanden, M.J., Boerner, P., Schrijver, C.J., Malanushenko, A.: 2013, Automated Temperature and Emission Measure Analysis of Coronal Loops and Active Regions Observed with the Atmospheric Imaging Assembly on the Solar Dynamics Observatory (SDO/AIA). *Solar Phys.* **283**(1), 5. DOI. ADS.
- Ballester, J.L.: 2005, Recent progress in prominence seismology. *Phil. Trans. Royal Soc. A* **364**(1839), 405. DOI.
- Berger, T.E., Shine, R.A., Slater, G.L., Tarbell, T.D., Title, A.M., Okamoto, T.J., Ichimoto, K., Katsukawa, Y., Suematsu, Y., Tsuneta, S., Lites, B.W., Shimizu, T.: 2008, Hinode SOT observations of solar quiescent prominence dynamics. *Astrophys. J.* **676**(1), L89. DOI.
- Chae, J., Ahn, K., Lim, E.-K., Choe, G.S., Sakurai, T.: 2008, Persistent horizontal flows and magnetic support of vertical threads in a quiescent prominence. *Astrophys. J.* **689**(1), L73. DOI.
- Diaz, A.J., Oliver, R., Ballester, J.L.: 2002, Fast magnetohydrodynamic oscillations in cylindrical prominence fibrils. *Astrophys. J.* **580**(1), 550. DOI.
- Edwin, P.M., Roberts, B.: 1983, Wave propagation in a magnetic cylinder. *Solar Phys.* **88**(1-2). DOI.
- Engvold, O.: 2007, *Observational aspects of prominence oscillations* **3**, Cambridge University Press (CUP), 152. DOI.
- Jing, J., Lee, J., Spirock, T.J., Wang, H.: 2006, Periodic motion along solar filaments. *Solar Phys.* **236**(1), 97. DOI.
- Kucera, T.A., Ofman, L., Tarbell, T.D.: 2018, Motions in prominence barbs observed on the solar limb. *Astrophys. J.* **859**(2), 121. DOI.
- Labrosse, N., Heinzel, P., Vial, J.-C., Kucera, T., Parenti, S., Gunár, S., Schmieder, B., Kilper, G.: 2010, Physics of solar prominences: I—spectral diagnostics and non-LTE modelling. *Space Sci. Rev.* **151**(4), 243. DOI.
- Lemen, J.R., Title, A.M., Akin, D.J., Boerner, P.F., Chou, C., Drake, J.F., Duncan, D.W., Edwards, C.G., Friedlaender, F.M., Heyman, G.F., Hurlburt, N.E., Katz, N.L., Kushner, G.D., Levay, M., Lindgren, R.W., Mathur, D.P., McFeaters, E.L., Mitchell, S., Rehse, R.A., Schrijver, C.J., Springer, L.A., Stern, R.A., Tarbell, T.D., Wuelser, J.-P., Wolfson, C.J., Yanari, C., Bookbinder, J.A., Cheimets, P.N., Caldwell, D., Deluca, E.E., Gates, R., Golub, L., Park, S., Podgorski, W.A., Bush, R.I., Scherrer, P.H., Gumm, M.A., Smith, P., Auken, G., Jerram, P., Pool, P., Soufli, R., Windt, D.L., Beardsley, S., Clapp, M., Lang, J., Waltham, N.: 2011, The atmospheric imaging assembly (AIA) on the solar dynamics observatory (SDO). *Solar Phys.* **275**(1-2), 17. DOI.
- Levens, P.J., Labrosse, N., Fletcher, L., Schmieder, B.: 2015, A solar tornado observed by EIS. *Astron. Astrophys.* **582**, A27. DOI.
- Levens, P.J., Schmieder, B., Labrosse, N., Ariste, A.L.: 2016, Structure of prominence legs: Plasma and magnetic field. *Astrophys. J.* **818**(1), 31. DOI.
- Li, X., Morgan, H., Leonard, D., Jeska, L.: 2012, A solar tornado observed by aia/sdo: Rotational flow and evolution of magnetic helicity in a prominence and cavity. *Astrophys. J.* **752**(2), L22. DOI.
- Lin, Y., rn Engvold, O., Wiik, J.E.: 2003, Counterstreaming in a large polar crown filament. *Solar Phys.* **216**(1/2), 109. DOI.

- Lin, Y., Engvold, O., van der Voort, L.H.M.R., van Noort, M.: 2007, Evidence of traveling waves in filament threads. *Solar Phys.* **246**(1), 65. [DOI](#).
- Lin, Y., Soler, R., Engvold, O., Ballester, J.L., Langangen, Ø., Oliver, R., van der Voort, L.H.M.R.: 2009, Swaying threads of a solar filament. *Astrophys. J.* **704**(1), 870. [DOI](#).
- Nakariakov, V.M., Ofman, L.: 2001, Determination of the coronal magnetic field by coronal loop oscillations. *Astron. Astrophys.* **372**(3), L53. [DOI](#).
- Okamoto, T.J., Liu, W., Tsuneta, S.: 2016, Helical motions of fine-structure prominence threads observed by hinode and iris. *Astrophys. J.* **831**(2), 126. [DOI](#).
- Okamoto, T.J., Tsuneta, S., Berger, T.E., Ichimoto, K., Katsukawa, Y., Lites, B.W., Nagata, S., Shibata, K., Shimizu, T., Shine, R.A., Suematsu, Y., Tarbell, T.D., Title, A.M.: 2007, Coronal transverse magnetohydrodynamic waves in a solar prominence. *Science* **318**(5856), 1577. [DOI](#).
- Oliver, R., Ballester, J.L.: 2002, Oscillations in quiescent solar prominences observations and theory – (invited review). *Solar Phys.* **206**(1), 45. [DOI](#).
- Panesar, N.K., Innes, D.E., Tiwari, S.K., Low, B.C.: 2013, A solar tornado triggered by flares? *Astron. Astrophys.* **549**, A105. [DOI](#).
- Pontieu, B.D., Title, A.M., Lemen, J.R., Kushner, G.D., Akin, D.J., Allard, B., Berger, T., Boerner, P., Cheung, M., Chou, C., Drake, J.F., Duncan, D.W., Freeland, S., Heyman, G.F., Hoffman, C., Hurlburt, N.E., Lindgren, R.W., Mathur, D., Rehse, R., Sabolish, D., Seguin, R., Schrijver, C.J., Tarbell, T.D., Wülser, J.-P., Wolfson, C.J., Yanari, C., Mudge, J., Nguyen-Phuc, N., Timmons, R., van Bezooijen, R., Weingrod, I., Brookner, R., Butcher, G., Dougherty, B., Eder, J., Knagenhjelm, V., Larsen, S., Mansir, D., Phan, L., Boyle, P., Cheimets, P.N., DeLuca, E.E., Golub, L., Gates, R., Hertz, E., McKillop, S., Park, S., Perry, T., Podgorski, W.A., Reeves, K., Saar, S., Testa, P., Tian, H., Weber, M., Dunn, C., Eccles, S., Jaeggli, S.A., Kankelborg, C.C., Mashburn, K., Pust, N., Springer, L., Carvalho, R., Kleint, L., Marmie, J., Mazmanian, E., Pereira, T.M.D., Sawyer, S., Strong, J., Worden, S.P., Carlsson, M., Hansteen, V.H., Leenaarts, J., Wiesmann, M., Aloise, J., Chu, K.-C., Bush, R.I., Scherrer, P.H., Brekke, P., Martinez-Sykora, J., Lites, B.W., McIntosh, S.W., Uitenbroek, H., Okamoto, T.J., Gummin, M.A., Auker, G., Jerram, P., Pool, P., Waltham, N.: 2014, The interface region imaging spectrograph (IRIS). *Solar Phys.* **289**(7), 2733. [DOI](#).
- Schmieder, B., Kucera, T.A., Knizhnik, K., Luna, M., Lopez-Ariste, A., Toot, D.: 2013, Propagating waves transverse to the magnetic field in a solar prominence. *Astrophys. J.* **777**(2), 108. [DOI](#).
- Schmieder, B., Tian, H., Kucera, T., Ariste, A.L., Mein, N., Mein, P., Dalmasse, K., Golub, L.: 2014, Open questions on prominences from coordinated observations by IRIS, hinode, SDO/AIA, THEMIS, and the meudon/MSDP. *Astron. Astrophys.* **569**, A85. [DOI](#).
- Su, Y., Wang, T., Veronig, A., Temmer, M., Gan, W.: 2012, Solar magnetized “tornadoes:” relation to filaments. *Astrophys. J.* **756**(2), L41. [DOI](#).
- Su, Y., Gömöry, P., Veronig, A., Temmer, M., Wang, T., Vanninathan, K., Gan, W., Li, Y.: 2014, Solar Magnetized Tornadoes: Rotational Motion in a Tornado-like Prominence. *Astrophys. J.* **785**(1), L2. [DOI](#). [ADS](#).
- Terradas, J., Arregui, I., Oliver, R., Ballester, J.L.: 2008, Transverse oscillations of flowing prominence threads observed with hinode. *Astrophys. J.* **678**(2), L153. [DOI](#).
- Torrence, C., Compo, G.P.: 1998, A practical guide to wavelet analysis. *Bul. American Meteor. Soc.* **79**(1), 61. [DOI](#).
- Welsch, B.T., Fisher, G.H., Abbett, W.P., Regnier, S.: 2004, ILCT: Recovering photospheric velocities from magnetograms by combining the induction equation with local correlation tracking. *Astrophys. J.* **610**(2), 1148. [DOI](#).
- Zirker, J.B., Engvold, O., Martin, S.F.: 1998, Counter-streaming gas flows in solar prominences as evidence for vertical magnetic fields. *Nature* **396**(6710), 440. [DOI](#).